LA-UR-16-27585
Approved for public release; distribution is unlimited.

Title: A physics-based crystallographic modeling framework for describing the thermal creep behavior of Fe-Cr alloys

Author(s): Wen, Wei
Capolungo, Laurent
Patra, Anirban
Tome, Carlos

Intended for: Report

Issued: 2017-02-02 (rev.1)

A physics-based crystallographic modeling framework for describing the thermal creep behavior of Fe-Cr alloys

Wei Wen, Laurent Capolungo, Anirban Patra, Carlos Tomé

Materials Science and Technology Division, Los Alamos National Laboratory
Los Alamos, NM 87544

Note: This Report addresses the Milestone M2MS-16LA0501032 of NEAMS Program ("Develop hardening model for FeCrAl cladding), with a deadline of 09/30/2016. Here we report a constitutive law for thermal creep of FeCrAl. This Report adds to and complements the one for Milestone M3MS-16LA0501034 ("Interface hardening models with MOOSE-BISON"), where we presented a hardening law for irradiated FeCrAl. The last component of our polycrystal-based constitutive behavior, namely, an irradiation creep model for FeCrAl, will be developed as part of the FY17 Milestones, and the three regimes will be coupled and interfaced with MOOSE-BISON.

1 Introduction

The development and use of high-performance Cr based steels alloys, with superior high temperature creep behavior, have been instrumental in improving the efficiency of thermal power plants [1–8]. Indeed, operation temperatures above 600^{o}C have been reached thanks, in particular, to the use of 9-12% Cr steels as boiler tubes and steam pipes. In parallel, other high Cr steel grades such as Fe-Cr-Al and modified Grade 91 (Fe-9Cr-1Mo) additionally exhibit low swelling during irradiation. Naturally, they are thus considered as candidate material systems for various nuclear energy applications (e.g. cladding). Their advanced oxidation resistance and high-temperature creep properties could prolong the service life and enhance the accident tolerance of both light water reactors (LWRs) and very-high-temperature reactors (VHTRs) [9–14]. Under such high temperature (e.g.), stress (e.g.) and irradiation environments, the materials microstructure and part geometry will degrade over time. Both thermal and irradiation creep largely contribute to the degradation process. Focus is placed here on thermal creep.

Over the past two decades, a series of studies have aimed at establishing a connection between the thermal creep behavior of high Cr steels and the specifics of their microstructures [1–7,13,15,16]. Following thermo-mechanical processing (e.g. tempering, tube extrusion), a polycrystalline sample will typically be textured, with most grains containing subgrain boundaries consisting of both geometrically necessary dislocations and $M_{23}C_6$ carbide (M=Cr). The latter also decorate grain boundaries. $M_{23}C_6$ carbide can stabilize the subgrain structure by obstructing the dislocation annihilation in the cell walls and hence decelerate the growth of subgrains [7,17] Finally, the microstructure contains an additional level of complexity as subgrains also contain carbo-nitride precipitates MX (M=V or Nb; X=C or N). In consequence, precipitation hardening and precipitation-enhanced subgrain boundary hardening have been suggested to be the most important creep strengthening mechanisms in high Cr steels [1].

As a consequence of the complex microstructure, the creep rate is controlled by a

broad spectrum of simultaneously active deformation mechanism (dissipative processes). Indeed. During thermal creep, plastic strain is likely to result from the activation of both diffusion creep and dislocation motion. The relative contribution of each depends on the imposed stress state, the internal stress state and temperature. Vacancy driven diffusion creep processes, such as the Nabarro-Herring creep and Coble creep, tend to play an important role in the high-temperature regime [13,18]. Shrestha et al. [13] show that the diffusion creep is dominant for the modified 9Cr-1Mo steel at 600ºC with creep stress lower than 60MPa. According to Ashby's map, dislocation motion is active in F82H steel (Fe-8Cr-2WVTa) for tensile stress above 100MPa at 600ºC.

Hardening will result from the interaction between moving dislocations and precipitates, subgrain boundaries, and other dislocations). The rate at which dislocation can overcome obstacles (via cross-slip, climb, unzipping) will be the limiting factor for the creep rate [19–22]. Finally, as dislocations interact with subgrain boundaries and as different species migrate, both precipitate coarsening and subgrain growth can be activated [2,6,17,23,24].

Polycrystal models can unravel the relative contribution of all dissipative processes. In an early work, Estrin and Mecking [25] developed a model assuming the average dislocation density is the sole structure factor affecting the mechanical response. This model, which is a unified description for both dynamic loading and creep tests, has been extended later to consider the particle coarsening [26]. The contributions of the subgrain structure were analyzed in the model of Gottstein and Argon [27]. It is concluded that the cross-slip, climb and migration of subgrain boundaries play a major role in the dislocation annihilation process. Roters et al. [28] divided the dislocations in the subgrain interior into mobile and immobile subsets based on the notion that the moving dislocations may be immobilized due to the formation of locks. The size of the second-phase particle is also included in determining the hardening behavior and meaning spacing of obstacles. The above models mainly focus on the evolution of dislocation populations. The studies are also carried out on the bypass mechanisms for the moving dislocations, i.e. [19,21,29,30]. Xiang and Srolovitz [29] performed the dislocation dynamic simulation on this subject. The results show that the dislocation climb can significantly facility the bypass for the impenetrable obstacles. Artz et al. [19] proposed a modeling analysis for the climb-over process. It is suggested that an extra detachment process may be required before the bypass due to the attractive interaction between the climbing dislocations and the particles.

The present work proposes a physics-based constitutive model, capable of predicting the mechanical response of the polycrystals and of evaluating the contribution of each mechanism during thermal creep of high Cr steels. In this model, thermal-activated dislocation glide and climb mechanisms are coupled and their activation controlled by transition state theory. In addition, in the approach proposed, the activation of climb is explicitly driven by the vacancy flux towards and away from dislocations. As stated in the above, the local stress states -within the activation volume corresponding to the process described- determines the likelihood of successfully activation. Therefore, the model presented, uses a recently proposed framework, to account for the distribution of internal stresses at a sub-material point scale. This added feature also allows selectively activating distinct dislocation recovery processes (i.e. dislocation annihilation within subgrains and in subgrain boundaries). The constitutive law proposed is embedded a mean-field visco-plastic framework (VPSC) [31,32]. The

model is employed to predict the behavior of the modified 9Cr-1Mo alloy under thermal creep tests with various temperatures and stresses. The predicted results are in a fairly good agreement with the experimental data. Among others, it is suggested that dislocation recovery within the subgrain could play a dominant role in the strain rate evolution observed during creep tests.

The study is structured as follows. A detailed description of the proposed thermal creep model will be given in Section 2 including the modeling background, the formulations to determine the creep shear rate on each slip system and a brief introduction of the VPSC framework. In Section 3, the predicted thermal creep behaviors are presented and compared with the experimental data provided by Basirat et al. [14] for Fe-9Cr-1Mo steel under various temperatures and applied stresses. The studies on the contributions of the mechanisms and the parameter sensitivities are also proposed. Section 4 presents a discussion of the role of each dislocation recovery process on the stress dependence of the creep rate.

2 Modeling framework

2.1 Microstructure and considered mechanisms

A paradigm microstructure, with features characteristic of high Cr alloys and schematically presented in Fig. 1, is chosen as the foundation of this model. This is the typical microstructure for heat treated and thermo-mechanically processed high Cr steels [1,3,6,13]. As shown, each grain contains a number of elongated subgrains which boundaries are denoted with dotted lines. Each subgrain contains a high density of dislocations (~$10^{14}m^{-2}$). Within subgrains quasi-spherical MX precipitates are considered to be randomly dispersed. According to Refs [6,33], the average size of MX particles is around 20-50*nm*, with mean inter-spacing in the order of 300*nm*. Larger rod-like $M_{23}C_6$ precipitates (100-300*nm*) are located mainly in the grain and subgrain boundaries.

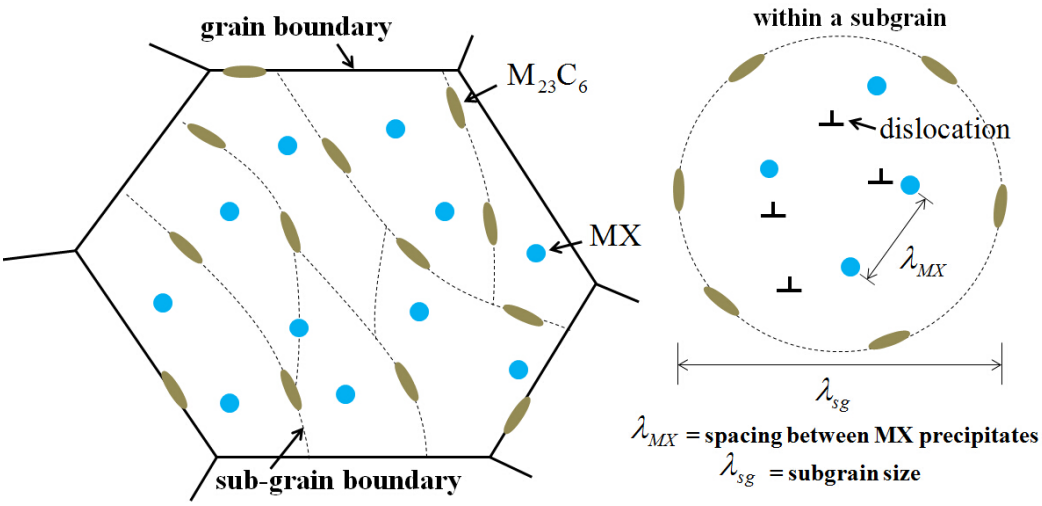

Fig. 1. Schematic view of the microstructure for heat treated high Cr steels.

With this microstructure, it is foreseen that dislocation motion is completely

arrested at subgrain boundaries and that dislocation transmission across the boundary is unlikely. Indeed subgrain boundaries typically exhibit a low angle misorientation and therefore contain a relatively packed wall of primary subgrain boundary dislocations such that a treatment of glide dislocation/subgrain boundary dislocation is preferable. In this work, the dislocations are divided into two subsets: the dislocations in the subgrain interior and in the cell walls. The plastic deformation is provided by the motion of the dislocations within subgrains. They may be mobilized or immobilized depending on the local stress state (see section 2.2). Importantly, one notes that subgrains are expected to have a complex stress state resulting from that of the dislocation and precipitates they contain but also from the long-range stress field arising from the primary dislocation network and rod-like precipitates within the subgrain boundaries.

Within subgrains, two types of obstacles to dislocation motion are considered: MX precipitates and other dislocations within the cell. The dislocation mobility will be determined by the dislocation waiting time at both type of obstacles before the bypass. Stored dislocations can overcome MX precipitates via either a thermally-activated glide (unzip from junctions and Orowan bypass mechanism for incoherent precipitates) or a climb assisted glide process depicted in Fig. 2. The climb process is non-conservative and therefore is rate limited by the vacancy flux towards or away from the dislocation [19–22].

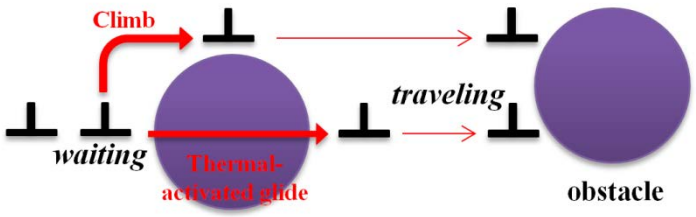

Fig. 2. Schematic view of the obstacle-bypass mechanisms for moving dislocations.

The evolution of the dislocation population within the subgrain is complex as the following processes are simultaneously active: (i) dislocation generation; (ii) dynamic recovery resulting from the short range interaction with other dislocations; (iii) trapping in the subgrain boundaries. The dislocations population in the cell wall can also reconfigure itself with time. It is postulated here that annihilation due to climb is a dominant feature. Technically the dislocation annihilation in the cell wall should result in a change in the subgrain size, and hence affect the mechanical response. However, this process is not considered here due to the lack of related statistical information. In addition, within the temperature and stress regimes considered (600-700^{o}C, $\geq$80MPa), diffusion creep and precipitate coarsening are neglected.

2.2 Constitutive law

The proposed model deals with the mechanical behavior at material point level. Within the paradigm microstructure, a material point will represent a grain containing a number of subgrains. The stress distribution within a material point is heterogeneous.

Theoretically, each material point can be decomposed into infinite sub-material points. The stress state is different at each point depending on the local dislocation arrangement. Some dislocations within the subgrain may be able to overcome the obstacles and keep gliding, whereas others will be immobilized due to the low stress state acting on them. However, effective medium models such as the VPSC model used in this work determine the inclusion-matrix interaction assuming the state inside the inclusion to be homogenous. Therefore, the mean mechanical response for each material point is necessary.

Using a crystal plasticity formalism, the plastic strain rate at the material point scale can be written as the sum of the shear strain rates on all potentially active slip systems as follows:

$$\dot{\varepsilon}_{ij}^{p} = \sum_{s} m_{ij}^{s} \bar{\dot{\gamma}}^{s} \tag{1}$$

Here $m_{ij}^{s} = \frac{1}{2}\left(n_i^s b_j^s + n_j^s b_i^s\right)$ is the symmetric Schmid tensor associated with slip system *s* in a material point p; $\boldsymbol{n}^s$ and $\boldsymbol{b}^s$ are the normal and Burgers vectors of this system. $\bar{\dot{\gamma}}^{s}$ denotes the mean shear rate in one material point. According to Wang et al. [34,35] the latter is given by an integral over all the local shear rates weighted by the volume fraction of the sub-material point. In the calculation, a probability distribution function P is used to represent the volume fraction distribution of sub-material points with a resolved shear stress (τ^s). *P* is referred to the average resolved shear of the material point ($\bar{\tau}^s$):

$$\bar{\dot{\gamma}}^{s} = \int_{-\infty}^{\infty} \dot{\gamma}^{s}(\tau^{s}) P(\tau^{s} - \bar{\tau}^{s}) d\tau^{s} \tag{2}$$

where $\bar{\tau}^s = \boldsymbol{\sigma} : \boldsymbol{m}$ with $\boldsymbol{\sigma}$ being the deviatoric stress of the material point. $\dot{\gamma}^s$ represents the shear rate of a sub-material point. P is described by the Gaussian distribution function:

$$P(\tau^{s} - \bar{\tau}^{s}) = \frac{1}{\sqrt{2\pi V}} \exp\left(-\frac{\left(\tau^{s} - \bar{\tau}^{s}\right)^2}{2V} \right) \tag{3}$$

V is the variance of the resolved shear stress, which is linked to the dislocation density [34,35]. Therefore, technically it should be different for each slip system and vary during the deformation. In this study, we assume *V* is equal for all systems since the initial status of dislocation arrangement is not completely known. Moreover, *V* is considered as constant throughout the creep tests. The decrease of dislocation density during creep will lead to a lower *V* value, and hence will further reduce the shear rate. However, this effect is out of the scope of the present work.

In the proposed model, the creep strain is accumulated due to the motion of the dislocations in the interior of the subgrains. The shear rate at each sub-material point can be expressed by the Orowan's equation as:

$$\dot{\gamma}^{s} = \rho_{cell}^{s} b v^{s} \cdot \mathrm{sign}(\bar{\tau}^{s}) \tag{4}$$

where ρ_{cell}^{s} is the density of dislocations within the subgrains. b is the magnitude of

the Burgers vector, and v^s is the mean velocity of dislocations traveling between barriers. As mentioned above, in this modeling framework, all the dislocations in the cell are considered as 'mobile' but with different mobility. The dislocations in a sub-material point will be effectively immobilized if the corresponding dislocation velocity is extremely low. The contribution of such a sub-material point is scaled by its volume fraction via $P(\tau^s - \overline{\tau}^s)$.

The mean dislocation velocity is given by the dislocation mean free path between obstacles λ^s, divided the time spent in this process. The latter includes the time traveling between obstacles t_t^s and the average time a dislocation spends waiting at an obstacle t_w^s [36–38]:

$$v^s = \frac{\lambda^s}{t_t^s + t_w^s} \tag{5}$$

The presence of multiple types of obstacles leads to a reduce in the mean free path. Generally, λ^s can be expressed as the geometric mean of the interspacing for individual obstacles:

$$\frac{1}{\lambda^s} = \frac{1}{\lambda_{\rho,cell}^s} + \frac{1}{\lambda_{MX}^s} \tag{6}$$

with $\lambda_{\rho,cell}^s$ and λ_{MX}^s denote the dislocation mean free path for dislocation obstacles and MX precipitates, respectively. The obstacle interspacing determination depends on the nature of barrier. It is suggested that the $\lambda_{\rho,cell}^s$ is inversely proportional to the hardening contribution of the dislocations in the cell, as $\tau_{\rho,cell}^s \propto \mu b / \lambda_{\rho,cell}^s$. A common method to express strengthening due to dislocation type obstacles is through the Taylor law. To describe the latent hardening associated with dislocation-dislocation interactions between slip systems, an extended form is used in this work as:

$$\tau_{\rho,cell}^s = \mu b \sqrt{\sum_{s} \alpha^{ss'} \rho_{cell}^{s'}} \tag{7}$$

Therefore, it gives:

$$\frac{1}{\lambda_{\rho,cell}^s} = \sqrt{\sum_{s} \alpha^{ss'} \rho_{cell}^{s'}} \tag{8}$$

$\alpha^{ss'}$ is the effective latent hardening matrix. The interspacing for MX precipitates is written in a simple form derived from the geometrical configuration of the obstacles on the slip plane [22,40,41].

$$\frac{1}{\lambda_{MX}^s} = h_{MX} \sqrt{N_{MX} d_{MX}} \tag{9}$$

here h_{MX} is the trapping coefficient for MX precipitate. N_{MX} and d_{MX} denote the number density and size of MX precipitates. This method is appropriate for hard obstacles [42], such as MX precipitates. Friedel [43] proposed an alternative expression for attractive obstacles on the glide plane, which is more suitable for weak obstacles.

In Eq. 5 the traveling time is given by $t_t^s = L^s / v_t$. Here v_t is the dislocation traveling velocity which is assumed to be equal to the shear wave velocity C_s (independent of the driving force) since the traveling time is negligible compared to the waiting time. It can be determined by $v_t \approx C_s = \sqrt{\mu/\rho_0}$ [38,44] where ρ_0 is the mass density and μ is the shear modulus given by $\mu = 103572MPa - T \cdot 48\,MPa/K$ [45].

To determine the dislocation average waiting time, we define the theoretical waiting times of thermally-activated glide ($t_{w,g}$) and climb ($t_{w,c}$) which represent the waiting times for the isolated mechanism. These two mechanisms, however, occur simultaneously, which can effectively reduce the waiting time. Therefore the waiting time at the obstacle type i (other dislocations, $i = \rho$ or MX precipitates, $i = MX$) within a sub-material point can be expressed using the harmonic mean:

$$\frac{1}{t_{w,i}^s} = \frac{1}{t_{w,g,i}^s} + \frac{1}{t_{w,c,i}^s} \tag{10}$$

The mean waiting time of slip system s when both obstacles are considered is given by the average of $t_{w,\rho}^s$ and $t_{w,\mathrm{MX}}^s$, weighted by the probability that the individual type of obstacle is encountered by the moving dislocation:

$$t_w^s = P_\rho t_{w,\rho}^s + (1 - P_\rho) t_{w,MX}^s \tag{11}$$

P_ρ is the probability that a dislocation encounters other dislocation and $1 - P_\rho$ that it encounters MX precipitates. Statistically, the inverse of the mean free path represents the number of obstacles per unit length along the gliding direction. In this way, the ratio of dislocation type obstacles in the corresponding section can be determined by the proportion between $1/\lambda_\rho^s$ and $1/\lambda^s$. Connecting with Eqs. 6-9, we will have:

$$P_\rho = \frac{1/\lambda_\rho^s}{1/\lambda^s} = \frac{\sqrt{\sum_s \alpha^{ss'} \rho_{cell}^{s'}}}{\sqrt{\sum_s \alpha^{ss'} \rho_{cell}^{s'}} + h_{MX}\sqrt{N_{MX} d_{MX}}} \tag{12}$$

2.2.1 Thermally-activated glide

The thermally activated glide describes the obstacle bypass processes including the unzipping of the junctions and the Orowan mechanism for large size particles. The MX precipitates are incoherent with the matrix and therefore impenetrable. In this case, the bypass at low-stress states is unlikely. However, under high driving stress, the dislocation can bow out between the MX precipitates, merge on the other side of the obstacle and continue to glide. The bypass for both types of obstacles can be considered as thermally-activated process. Therefore, $t_{w,g,MX}^s$ and $t_{w,g,\rho}^s$ can be described using the Kocks-type activation enthalpy law [36,38,46] but with different values for the attempt frequencies and activation energies:

$$\frac{1}{t_{w,g,i}^s} = \frac{\upsilon_{G,i}^s}{\exp\left(\dfrac{\Delta G_i^s}{kT}\right)} \tag{13}$$

In Eq. 13, i refers to different types of obstacles (dislocations or MX precipitates). $\upsilon_{G,i}^{s}$, k and T are the effective attempt frequency, Boltzmann constant and absolute temperature, respectively. ΔG_i^s denotes the activation energy given by:

$$\Delta G_i^s = \begin{cases} \Delta G_{0,i}\left(1-\left(\dfrac{\left|\tau^s\right|}{\tau_c^s}\right)^p\right)^q & if\ \left|\tau^s\right| < \tau_c^s \\ 0 & if\ \left|\tau^s\right| \geq \tau_c^s \end{cases} \tag{14}$$

where $\Delta G_{0,i}$ is activation energy without any external stress applied. Its value is dependent on the nature of the obstacle, such as the dislocation interaction and the strength and size of precipitates. p $(0 < p \leq 1)$ and q $(1 \leq p < 2)$ are the exponent parameters in the phenomenological relation determining the shape of the obstacles resistance profile [46]. τ_c^s is the Critical Resolved Shear Stress (CRSS). The hardening contributions from the dislocations in the subgrain and MX precipitates, as well as the $M_{23}C_6$ precipitates and the dislocations in the cell wall due to the long term stress field.

The long-range hardening induced by multiple sources has been studied in many works i.e. [40,47,48]. A commonly used superposition principle is written as:

$$\tau_t^m = \tau_1^m + \tau_2^m \tag{15}$$

τ_1 and τ_2 are the hardening due to source 1 and 2, respectively. τ_t denotes the superimposed hardening. The exponent m varies between 1 and 2 depending on the hardening mechanisms. The value higher than 2 is also reported for irradiation-induced defects [40]. The long range hardening sources within the microstructure paradigm include the MX precipitates, $M_{23}C_6$ carbides and the dislocations. Notice that the dislocations comprise two populations: the ones within the subgrains and the ones in subgrain boundaries. Both of them contribute to the hardening due to the long range stress field with similar features. Consequently, it is reasonable to consider them as one individual hardening source. As mentioned above, the hardening due to dislocation can be obtained using the complex form of the Taylor law:

$$\tau_\rho^s = \mu b \sqrt{\sum_{s} \alpha^{ss'}\left(\rho_{cell}^{s'} + \rho_{cw}^{s'}\right)} \tag{16}$$

The precipitate hardening should superimpose with τ_ρ^s using the principle in Eq. 15. Moreover, the linear superimposition is restricted if one of the hardening sources is the intrinsic frictional resistance τ_0^s [40,47,48]. Therefore, the total CRSS is given by:

$$\tau_c^s = \tau_0^s + \left(\left(\tau_\rho^s\right)^m + \left(\tau_P^s\right)^m\right)^{1/m} \tag{17}$$

τ_P^s is the hardening contributions by both MX and $M_{23}C_6$ precipitates.

In this work, the attempt frequency for overcoming an MX precipitate is assumed to be constant. The one for junction unzipping process $\upsilon_{G,\rho}$ is suggested to be dependent on

the dislocation traveling velocity, an entropy factor χ (in the order of 1) and the average length of the vibrating dislocation segments (represented by the dislocation mean free path λ^s) [35,49].

$$\upsilon_{G,\rho} = \chi C_s / \lambda^s \tag{18}$$

2.2.2 Dislocation climb

Dislocation climb refers to the process that edge dislocations migrate perpendicular to the slip plane via point defect absorption/emission. This stress- and temperature-dependent mechanism may assist the edge dislocations to bypass the barriers during deformation. The effects of climb are more evident at high-temperature due to the high concentration and diffusivity of point defects [19–22]. In the present work, the concept of climb waiting time (Eq. 10) is introduced to describe this process. Notice that the activation of dislocation climb process will affect the mean dislocation mobility, but the sign of shear rate is only governed by the resolved shear stress, which captures the fact that the climb mechanism is assisting the dislocation glide.

The modeling of dislocation climb has been studied in many works i.e. [18,22,44,50–53]. The climb velocity depends on the climb driving force and on the flow of point defects into the edge dislocations. The climb component of Peach-Koehler force has been discussed in Refs. [54–58] and is essential to determine the climb rate on each slip system in a crystallographic framework. Notice that the climb may be a reaction-rate-controlled process or a diffusion-controlled process [18]. The former usually occurs in irradiated materials, where the current of defects entering and/or leaving the dislocation core are very large and reach the defect-dislocation reaction rate limit. Otherwise, climb is a diffusion-controlled process, such as in the thermal creep case. Some authors [18,44,50–53] determine the flux of vacancies through the gradient of the vacancy concentration in the dislocation control volume. The detailed description of this method is given in the Appendix. The net current of vacancies I_v^s for slip system *s* can be expressed as:

$$I_v^s = \frac{2\pi b D_v \left[C_v^\infty - C_v^0 \exp\left(\frac{-f_c^s \Omega}{kTb} \right) \right]}{\Omega b \ln(\mathrm{r}_\infty / \mathrm{r}_d)} \tag{19}$$

here $\Omega \approx b^3$ is the atomic volume. D_v is the vacancy diffusivity. C_v^0 is the equilibrium vacancy concentration at temperature T in the bulk of the crystal, given by $C_v^0 = \exp\left(S_f^v / k\right) \exp\left(-E_f^v / kT\right)$ [18]. E_f^v and S_f^v are the vacancy formation energy and entropy, respectively. C_v^∞ represents the vacancy concentration in the material matrix which is assumed to be equal to C_v^0 in the present work. f_c^s is the climb component of Peach-Koehler force [54–58]. r_d and r_∞ denote the radii of the inner and outer boundaries for the cylindrical control volume defined around the dislocation line. Therefore, the climb velocity is given by:

$$v_c^s = \frac{I_v^s \Omega}{b} = \frac{2\pi D_v \left[C_v^\infty - C_v^0 \exp\left(\frac{-f_c^s \Omega}{kTb} \right) \right]}{b \ln(\mathrm{r}_\infty / \mathrm{r}_d)} \tag{20}$$

The climb waiting time can be determined by the ratio between the mean climb velocity of the edge dislocation and the average distance to climb before the bypass [22]. In the present work, dislocation climb is assumed to occur for the bypass of both, dislocation and MX precipitate obstacles. Therefore, the average waiting time of climb for edge dislocation can be expressed as:

$$\frac{1}{t^s_{w,c,i}} = R_e \frac{\left|v^s_c\right|}{l_i} \tag{21}$$

The absolute value of v^s_c is used here because a dislocation can climb over the obstacle in both positive and negative directions. l_i represents the average climb distance to bypass the obstacles. R_e, denoting the proportion of edge dislocations, is introduced since only edge dislocations contributes to the climb process. In BCC structure, the nucleation of the double kink structure is frequent. The motion of the edge (or screw) dislocations will result in the elongation of the screw (or edge) dislocation kinks [44,59]. Since the edge dislocations glide much faster in BCC material, the density of edge dislocations is usually limited. In this work, $R_e = \rho_{edge} \big/ \rho = 10\%$ is estimated.

After the climb the dislocation needs to detach the particles before it can continue to glide. The attractive interaction between the climbing dislocation and particles has been reported in Arzt et al. [19,20], but is not included in the proposed model since for the Fe-Cr alloy is has not been studied in detail. Consequently, the climb rate for the precipitate obstacles may be overestimated in this work.

2.3 Dislocation density law

The dislocation density evolution plays a key role in the present thermal creep model. The variance of strain rate for the modified 9Cr-1Mo steel is mainly controlled by the evolution of the dislocation density in the subgrain [4]. The dislocation density evolution processes considered in this model for $\dot{\rho}^s_{cell}$ are dislocation generation ($\dot{\rho}^{s,+}_{cell,g}$), dynamic recovery due to multiple mechanisms ($\dot{\rho}^{s,-}_{cell,a}$) and trapping at the subgrain boundaries ($\dot{\rho}^{s,-}_{cell,trap}$):

$$\dot{\rho}^s_{cell} = \dot{\rho}^{s,+}_{cell,g} - \dot{\rho}^{s,-}_{cell,a} - \dot{\rho}^{s,-}_{cell,\mathrm{trap}} \tag{22}$$

The dislocation generation process concerns the expansion of the pinned dislocation segments. The generation rate is related to the area swept by the moving dislocations. The term $\dot{\rho}^{s,+}_{cell}$ is determined by a commonly used expression [60–62]:

$$\dot{\rho}^{s,+}_{cell,g} = \frac{k_1}{b\lambda^s}\left|\dot{\bar{\gamma}}^s\right| \tag{23}$$

The dynamic recovery process involves many mechanisms. The most important ones are suggested to be cross-slip and climb [24,63]. The moving dislocation can cross-slip and annihilate if it encounters a dislocation with opposite Burger vector. In the classic Kocks-Mecking law [63–66], the dynamic recovery term can be written as:

$$\dot{\rho}^{s,-}_{cell,a} = f\rho^s_{cell}\left|\dot{\bar{\gamma}}\right| \tag{24}$$

here f is the recovery parameter. It is suggested to be a function of temperature and strain rate [63–66]. In many works for the strain imposed plastic deformation with high applied stress, i.e. [62,66], this parameter is considered as weakly dependent on the strain rate (or completely insensitive). Estrin [63] indicated that the strain rate sensitivity of f is in fact associated with the dominant mechanism. Compared to cross-slip, the f parameter should be more sensitive to strain rate in the climb governed process. Estrin [63] also proposed a general expression for f as:

$$f = k_2 \left(\frac{\dot{\varepsilon}_0}{\dot{\varepsilon}} \right)^{\frac{1}{n_0}} \tag{25}$$

where $\dot{\varepsilon}_0$ is a reference strain rate and n_0 is related to the strain rate sensitivity. Its value should be around 3-5 for a climb dominant recovery, or higher if it is mainly controlled by cross-slip [63].

The statistical modeling of the trapping process usually suggests that the moving dislocation may be immobilized after it swept a certain area [22,38,67]. Therefore, the trapping term in the present model is given by:

$$\dot{\rho}^{s,-}_{cell,trap} = \frac{k_3}{\lambda_{sg}} \left| \dot{\bar{\gamma}} \right| \tag{26}$$

where the λ_{sg} represents the sub-grain size. As mentioned in section 2.1, λ_{sg} is assumed to be constant throughout the creep test in this work. In Eqs. 23-26, k_1, k_2 and k_3 are material constants.

The evolution of the dislocation density in the cell wall is determined through the trapping of the moving dislocations and the annihilation process, written as:

$$\dot{\rho}^{s}_{cw} = \dot{\rho}^{s,-}_{cell,\mathrm{trap}} - \dot{\rho}^{s,-}_{cw,a} \tag{27}$$

Different from the dynamic recovery in Eqs. 24 and 25, the annihilation in the cell wall is only controlled by climb since the trapped dislocations cannot glide [28]. Nes [24] suggested that the climb-only annihilation rate is proportional to the dislocation climb velocity and current dislocation density, and inversely proportional to the average dipole separation (l_g) as $\dot{\rho}^{s-}_{\mathrm{climb}} \propto \rho^s \left| v^s_c \right| / l_g$. l_g scales with $1/\sqrt{\rho^s_{cw}}$. Therefore:

$$\dot{\rho}^{s,-}_{cw,a} = k_c \left| v^s_c \right| \left(\rho^s_{cw} \right)^{\frac{3}{2}} \tag{28}$$

k_c is a material constant and the climb velocity v^s_c is given in Eq. 20.

2.4 Brief description of VPSC model

The detailed description of VPSC model can be found in Refs. [32,68]. In this work, the VPSC framework is used as a platform for calculating the interaction between the effective medium representing the macroscopic polycrystal and the individual grains. The self-consistent model treats each grain as an inhomogeneous visco-plastic inclusion embedded in the “homogeneous effective medium” (HEM) with the average properties

of all grains in the polycrystal. Deformation takes place either by enforcing a macroscopic deformation rate or imposing a stress for prescribed time increment. The latter case corresponds to creep. The plastic deformation in each grain occurs via the activation of slip systems. The total strain rate in one grain is given by the sum of the shear rates of all systems (Eq. 1). Its linearized form is written as:

$$\dot{\varepsilon}_{ij}^{g} = M_{ijkl}^{g}\sigma_{kl} + \dot{\varepsilon}_{ij}^{0,g} \tag{29}$$

where M_{ijkl}^{g} and $\dot{\varepsilon}_{ij}^{0,g}$ are the visco-plastic compliance and the back-extrapolated rate of grain g, respectively. M_{ijkl}^{g} should be calculated as [34]:

$$M_{ijkl}^{g} = \frac{\partial \dot{\varepsilon}_{ij}^{g}}{\partial \sigma_{kl}} = \sum_{s} \frac{\partial \dot{\bar{\gamma}}}{\partial \bar{\tau}^{s}} \frac{\partial \bar{\tau}^{s}}{\partial \sigma_{kl}} m_{ij} = \sum_{s} \frac{\partial \dot{\bar{\gamma}}}{\partial \bar{\tau}^{s}} m_{ij} m_{kl} \tag{30}$$

Similar to Eq. 29, the relationship between the strain rate and stress for the aggregate is expressed as a linearized form:

$$\dot{\bar{\varepsilon}}_{ij} = \bar{M}_{ijkl}\bar{\sigma}_{kl} + \dot{\bar{\varepsilon}}_{ij}^{0} \tag{31}$$

with $\dot{\bar{\varepsilon}}_{ij}$, $\bar{\sigma}_{kl}$, $\bar{M}_{ijkl}$, and $\dot{\bar{\varepsilon}}_{ij}^{0}$ denoting the macroscopic strain rate, stress, visco-plastic compliance tensor and back-extrapolated rate, respectively. The interaction between the single crystal and the surrounding effective medium in the VPSC model is expressed in the interaction law:

$$\dot{\varepsilon}_{ij}^{g} - \dot{\bar{\varepsilon}}_{ij} = -\tilde{M}_{ijkl}\left(\sigma_{kl}^{g} - \bar{\sigma}_{kl}\right) \tag{32}$$

The interaction tensor $\tilde{M}_{ijkl}$ takes into account the grain shape effect via the Eshelby tensor $\boldsymbol{S}$ as:

$$\tilde{M}_{ijkl} = \left(I - S\right)_{ijmn}^{-1} S_{mnpq}\bar{M}_{pqkl} \tag{33}$$

3 Simulation results and discussion

The experimental data used to evaluate the proposed model is provided by Basirat et al. [14] for the modified Fe-9Cr-1Mo alloy. Prior to the creep tests, this material has been normalized at 1038°C for 6h and tempered at 788°C for 43 min. The resulting microstructure (initial status for the tests) is consistent with the chosen paradigm (see section 2.1). The detailed description can be found in Ref [13] from the same group.

3.1 Parameter calibration and simulation conditions

The parameters involved in the simulations are discussed in this section. The affine interaction in the VPSC framework is used in this work. The average size of MX precipitates reported in Ref [13] is around 37 nm. The precipitate number density and trapping parameter are chosen to be 3×10^{20} m^{-3} and 1, respectively. This leads to the mean spacing $\lambda_{MX}^{s}=1/h_{MX}\sqrt{N_{MX}d_{MX}}\approx 300\,nm$. This value is in the reasonable range according to Ref [6].

In the hardening law, the dislocation-dislocation interaction parameters $\alpha^{ss'}$ are chosen based on the data in Ref. [69]. The hardening superposition factor m is set to 2 as given in Refs [40,47,48]. In the Kocks type law (Eqs. 13 and 14), the parameter $\Delta G_{0,\rho}$, $\Delta G_{0,MX}$, $\upsilon_{G,MX}$, p and q are obtained by back fitting the experimental data within their reasonable ranges ($\upsilon_{G,i}\approx 10^{10}\sim 10^{11}\ s^{-1}$ [22]; $0<p\le 1$ and $1\le p<2$ [46]).

The dislocation density in heat treated high Cr steels is of the order 10^{14} m^{-2} [14,70,71]. In this work, the initial values of ρ_{cell}^{s} and ρ_{cw}^{s} for each system are chosen to be $4\cdot10^{12}$ m^{-2} and $1\cdot10^{13}$ m^{-2}, respectively. Hence the total densities in the cell and in the cell wall start at $9.6\cdot10^{13}$ m^{-2} and $2.4\cdot10^{14}$ m^{-2}. The evolution related parameters k_1, k_2, k_3 and k_c are calibrated according to the experimental data. The strain rate sensitivity parameter n_0 in the dislocation dynamic recovery term depends on the annihilation mechanisms [24]. Its value is chosen to be 3.5 in this work and the rationale will be discussed in the following sections.

The vacancy diffusivity and the equilibrium concentration of vacancies are important parameters affecting the climb process. They are determined using molecular dynamics simulation data reported by Mendelev and Mishin [72] for BCC Fe. The diffusivity is calculated by:

$$D_v = D_v^0 \exp\left(-E_m^v/kT\right) \tag{34}$$

where the vacancy migration energy E_m^v is 0.6 eV and the diffusion constant D_v^0 is $7.87\times10^{-7}\ \mathrm{m^2/s}$. The vacancy formation energy and entropy are given as function of temperature:

$$E_f^v = g_0 - g_2 T^2 - 2g_3 T^3$$
$$S_f^v = -g_1 - 2g_2 T - 3g_3 T^2 \quad (35)$$

The g_x coefficients and the other parameters involved in the calculation of dislocation waiting time are listed in Table 1.

The simulation is carried out using the modeling framework described above. Since the cladding material exhibits a weak texture, an initial texture consisting of 100 random orientations (Fig. 4) is utilized as input. The $\{110\}\langle 111\rangle$ and $\{112\}\langle 111\rangle$ slip modes are assumed to be active in BCC Fe-Cr-Mo steel. The tensile creep tests are simulated under stress-controlled boundary conditions: stress along axis 3 (Σ_{33}) is imposed and the rest of the stress components Σ_{ij} are enforced to be zero.

The experimental data used to adjust and benchmark the proposed model is taken from available literature [14]. The same temperatures and creep stresses will be applied in the simulations. The results will be presented in section 3.3. Notice that only the primary creep stage and steady-state stage of thermal creep will be simulated. The third stage, where the creep rate shows an evident increase, is usually attributed to void nucleation and crack formation [39,73] and is out of the scope of the present modeling framework.

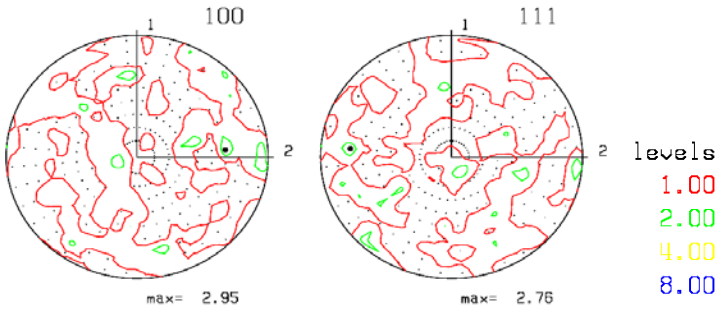

Fig. 3. Pole figures for the initial random texture with 100 grains.

Table 1. Parameters used for the Fe-Cr-Mo alloy in this work

Parameters	Fe-Cr-Mo	
ρ_0 (mass density)	8000 Kg/m^3	
b (magnitude of Burgers vector)	$2.48 \cdot 10^{-10}$ m	
μ (shear modulus)	103572 *MPa-T*·48*MPa/K*	[45]
N_{MX} (number density of MX precipitate)	$3 \cdot 10^{20}$ m^{-3}	[6]*
D_{MX} (average diameter of MX precipitate)	37 nm	[13]

h_{MX} (trapping coefficient for MX precipitates)	1	[6]*
τ_0 (friction stress)	0 *MPa*	
τ_{MX} (hardening contribution of MX precipitates)	365 *Mpa* (600ºC) 325 *Mpa* (650ºC) 315 *Mpa* (700ºC)	
m (exponent factor)	2	[40,47,48]
$\alpha_0^{ss'}$ (saturation dislocation-dislocation interaction)	0.7 ($s = s'$); 0.05 ($s \neq s'$)	[69]*
V (resolved shear stress variance)	1000 MPa^2	
$\Delta G_{0,\rho}$ (zero-stress activation energy for dislocations)	2.8 eV	
$\Delta G_{0,MX}$ (zero-stress activation energy for MX precipitates)	7 eV	[74]*
p (exponent parameter)	0.7	[46]*
q (exponent parameter)	1.4	[46]*
$\upsilon_{G,MX}$ (attack frequency for MX precipitate obstacle)	$1.3 \cdot 10^{10}$ s^{-1}	[22]*
R_e (proportion of edge dislocations)	10%	
χ (entropy factor)	1	[35]
r_d (inner radius of dislocation control volume)	4b	[50]
r_∞ (inner radius of dislocation control volume)	200b	
$\rho_{cell,0}^s$ (initial dislocation density in the cell)	$4 \cdot 10^{12}$ m^{-2}	[14,70,71]*
$\rho_{cw,0}^s$ (initial dislocation density in the cell wall)	$1 \cdot 10^{13}$ m^{-2}	[14,70,71]*
l_ρ (average distance to climb for dislocation obstacle)	100b	
k_1 (material constant)	0.12	
k_2 (material constant)	85	
k_3 (material constant)	$0.5 \cdot 10^9$	
k_c (material constant)	0.1	
n_0 (annihilation strain rate sensitivity)	3.5	
D_v^0 (diffusion constant)	$7.87 \cdot 10^{-7}$ m^2/s	[30]
E_m^v (vacancy migration energy)	0.6 eV	[30]
g_0 (coefficient used in Eq. 35)	1.724 eV	[30]
g_1 (coefficient used in Eq. 35)	$-1.2 \cdot 10^{-4}$ eV/K	[30]
g_2 (coefficient used in Eq. 35)	$-2.79 \cdot 10^{-8}$ eV/K^2	[30]
g_3 (coefficient used in Eq. 35)	$-5.93 \cdot 10^{-11}$ eV/K^3	[30]

* Parameter estimated or back-fitted from experimental data within the range given in the listed references.

3.2 Simulation results

The creep rate and the creep strain in Basirat et al. [14] are measured under the following conditions: 600ºC with 150 and 200 MPa; 650ºC with 150 and 200MPa; 700ºC with 80, 100, 150 and 200 MPa. Figs. 4-7 show the comparison of the predicted results with experiments as a function of stress and temperature. The most obvious feature in these experiments is the strong dependence of the creep rate with applied stress. Differences of 50 MPa or even 20 MPa impact strongly on the creep rates

observed. Despite such demanding experimental conditions, reasonable agreement is obtained for both. Notice that the experimental data in Basirat et al. show an obvious power-law regime behavior [13,14]. Therefore, the diffusion creep, which is excluded from this model, will not evidently affect the prediction in this work.

It can be seen that the simulation results capture the evolution for both the creep rate and creep strain curves over several orders of magnitudes. Still, some discrepancies are apparent in Figs. 4-7, the possible causes for which are discussed in what follows. First, a random texture is used in this work due to the lack of experimental texture data for both alloys. The effect of the initial texture will be discussed in section 3.4. Another possible source of error could be the initial dislocation densities used, which are the same for all tests in this work. However, they are likely to be different depending on the temperature, which will induce some annealing. The parameters controlling the waiting time of the thermal-activated glide and climb, could also affect the predicted results. These parameters can be better calibrated by using the data from more systematic experiments or low scale dislocation dynamic simulations.

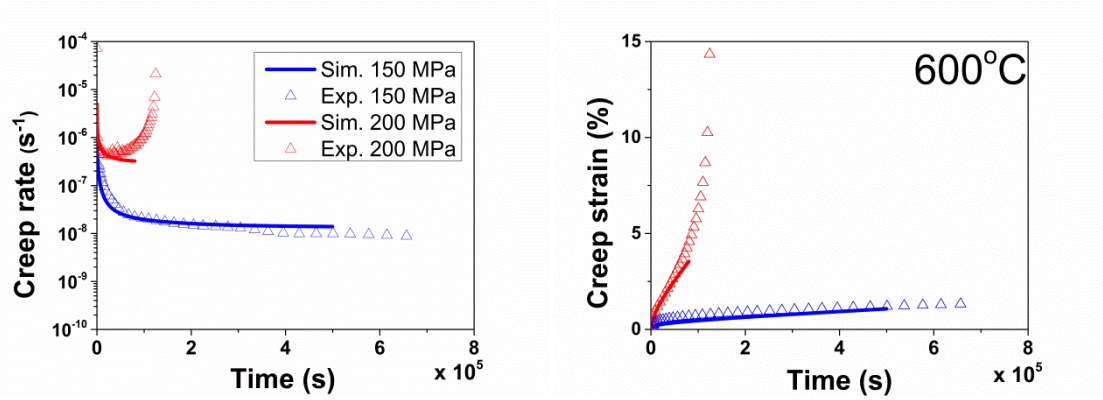

Fig. 4. Predicted creep rate (left) and creep strain (right) for Fe-Cr-Mo steel at 600ºC with applied stress of 150 and 200 MPa. Experimental data from Ref. [14].

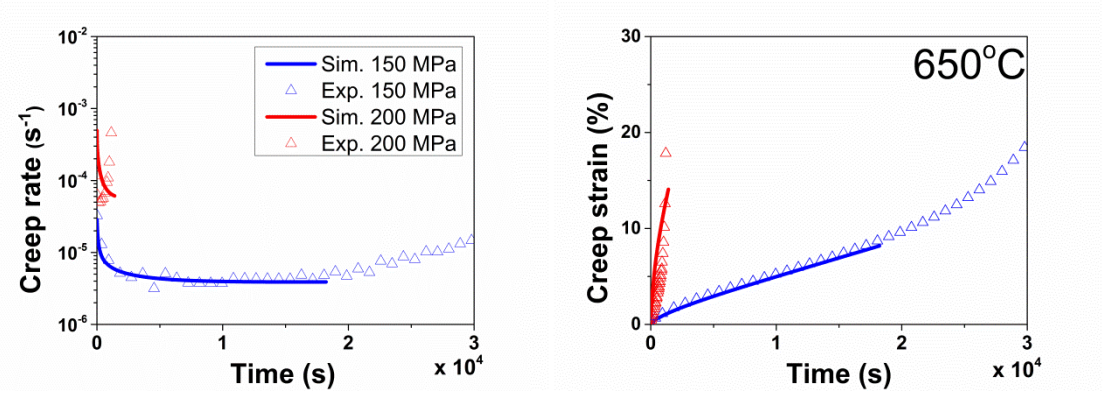

Fig. 5. Predicted creep rate (left) and creep strain (right) for Fe-Cr-Mo steel at 650ºC with applied stress of 150 and 200 MPa. Experimental data from Ref. [14].

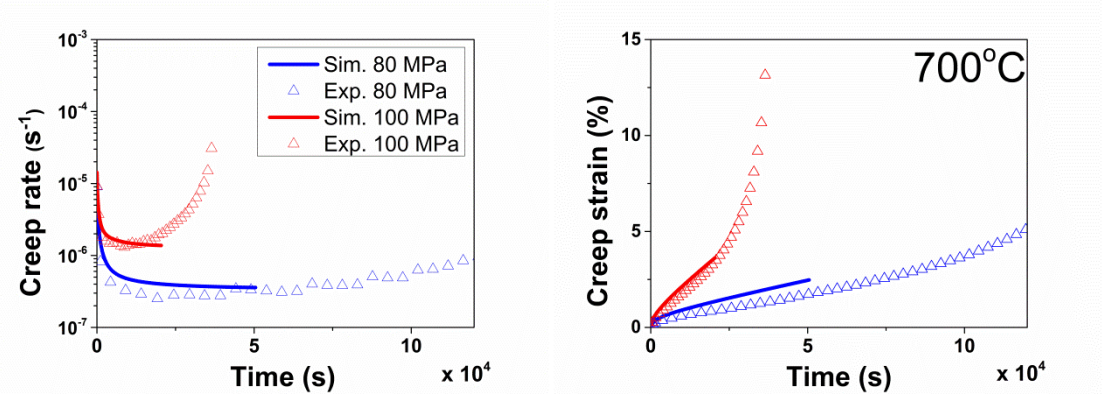

Fig. 6. Predicted creep rate (left) and creep strain (right) for Fe-Cr-Mo steel at 700°C with applied stress of 80 and 100 MPa. Experimental data from Ref. [14].

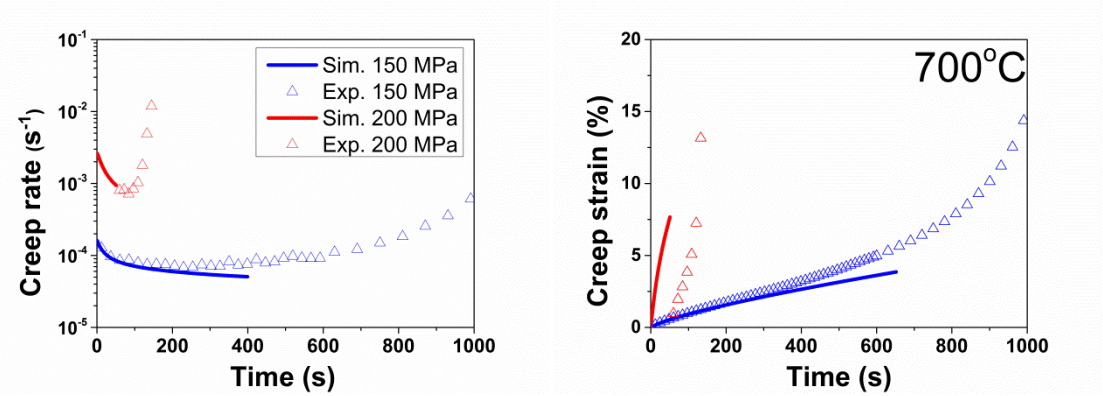

Fig. 7. Predicted creep rate (left) and creep strain (right) for Fe-Cr-Mo steel at 700°C with applied stress of 150 and 200 MPa. Experimental data from Ref. [14].

3.3 Relative contribution of glide and climb mechanisms

The proposed modeling framework is able to consider the contribution of both the thermally-activated glide and the dislocation climb mechanisms in the deformation process. In order to study their relative activities, we define $P_c = 1 - \varepsilon^i_{w/o} / \varepsilon^i_w$ to describe the percentage of the climb contribution. ε^i_w and $\varepsilon^i_{w/o}$ denote the creep rates at the initial step of the simulations with and without considering the climb mechanism (using the parameters of Fe-Cr-Mo steel given in section 3.1).

Fig. 8 exhibits the predicted relative contribution of climb under various temperature and stress. As shown in Fig. 8a, the climb mechanism contributes relatively more at lower temperature. In this model, the climb process is controlled by the temperature-dependent equilibrium vacancy concentration, vacancy diffusivity and the chemical force (see Appendix). The thermally-activated glide is also strongly dependent on temperature, which is mainly due to the temperature-dependent hardening. The results in Fig. 8a indicate that the thermally-activated glide is relatively more sensitive

to temperature than climb. Fig. 8b demonstrates that the relative activity of climb is inversely proportional to the creep stress. It can be explained as that the thermally-activated glide activity shows an exponential growth with the stress. On the other hand, the value of $f_c^s \Omega / kTb$ in Eqs. 19 and 20 is low (close to zero). This mathematically leads to a relatively more linear relationship between the climb velocity and the climb component of the P-K force [52].

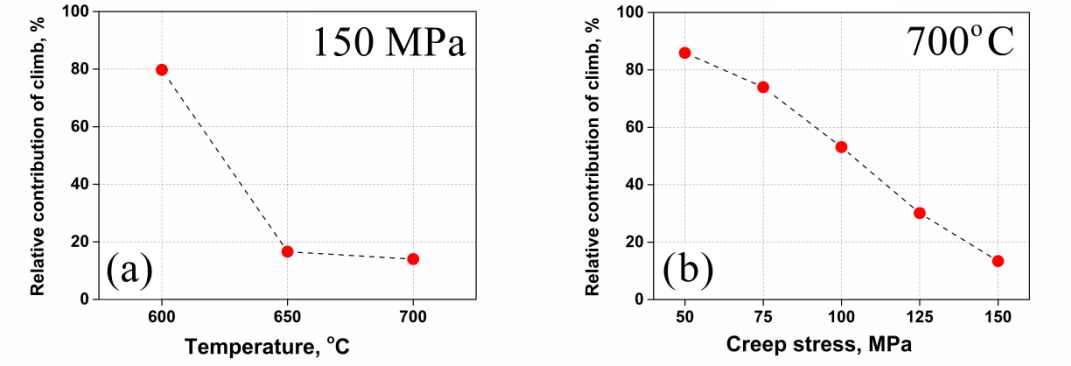

Fig. 8. Relative contribution of dislocation climb mechanism as a function of (a) temperature and (b) creep stress.

3.4 Dislocation density evolution

The predicted dislocation density evolution in the subgrain for the polycrystals are presented in Fig. 9. The results are compared for various loading condition. It shows that ρ_{cell} tends to decrease more for lower temperature and/or stress. On the other hand, the evolution of ρ_{cw}, given in Fig. 10, show the same tendency. Notice that the subgrain size, which is considered constant in this work, is actually dependent on ρ_{cw}. It has been reported that the saturation subgrain size, which scales with $1/\sqrt{\rho_{cw}}$, is inversely proportional to the applied stress [6]. This is in agreement with the present simulations.

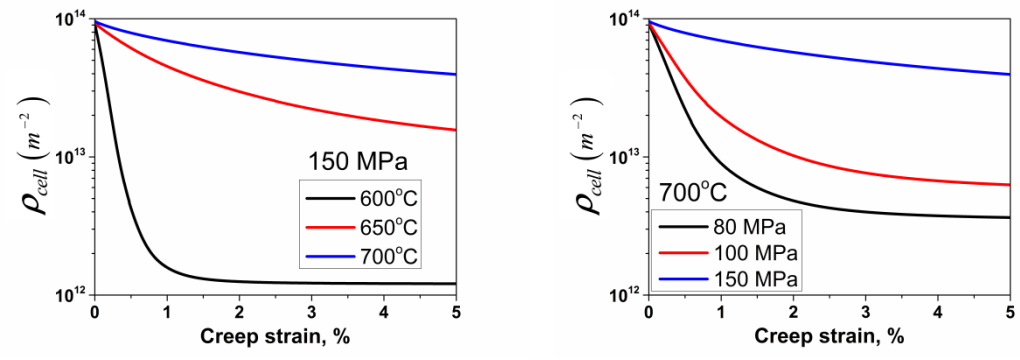

Fig.9. Predicted evolution of dislocation density within subgrains under different temperatures (left) and stresses (right)

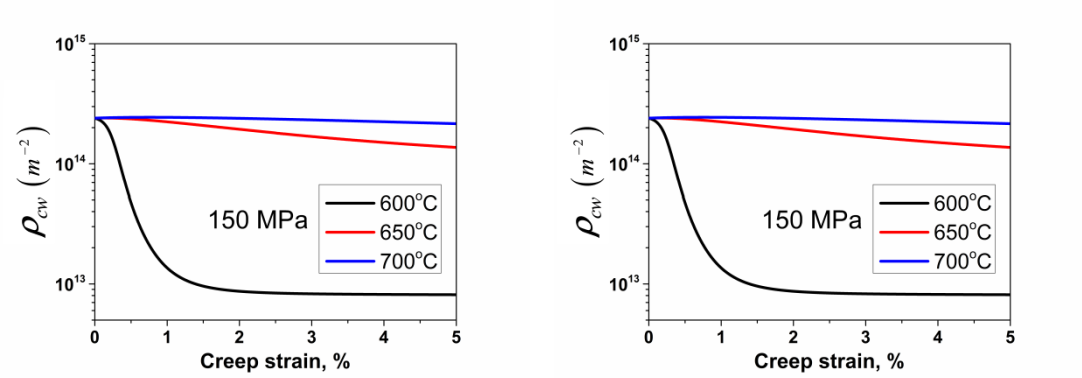

Fig.10. Predicted evolutions of dislocation density in the cell walls under different temperatures (left) and stresses (right)

In Fig. 11 the roles of each dislocation density evolution term ($\dot{\rho}^{s,+}_{cell,g}$, $\dot{\rho}^{s,-}_{cell,a}$, $\dot{\rho}^{s,-}_{cell,trap}$ and $\dot{\rho}^{s,-}_{cw,climb}$) are analyzed. By summing the components from individual slip systems and then averaging these values across all grains, the macroscopic $\dot{\rho}^{+}_{cell,g}$, $\dot{\rho}^{-}_{cell,a}$, $\dot{\rho}^{-}_{cell,trap}$ and $\dot{\rho}^{-}_{cw,climb}$ are calculated for the polycrystal. For lower stress and temperature cases, we can see that the value for $\dot{\rho}^{-}_{cell,a}$ is relatively high at the beginning of the tests. This indicates that the dynamic recovery process dominates the drop of ρ_{cell} (and hence the creep rate) in the primary creep regime. This term later becomes very weak in the steady state due to the large decrease of the ρ_{cell} and creep rate.

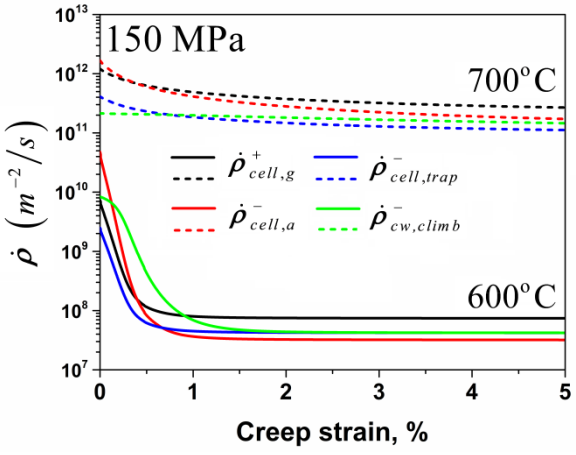

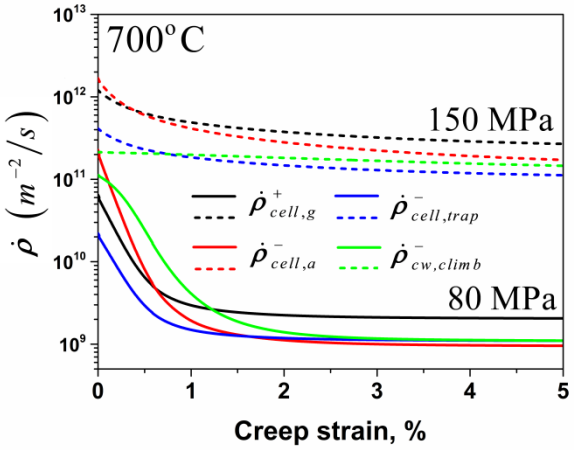

Fig.11. Contribution for the dislocation density evolution related mechanisms for different temperatures (top) and stresses (bottom).

The experimental data used in this work [14] show an important dependence of the creep rate evolution with stress and temperature. In Fig. 12, some of the experimental creep rate curves are presented for different stresses and temperatures. The strain rate data are normalized by the initial strain rate in the experimental data $\dot{\varepsilon}^{i}_{\exp}$, whereas the time is normalized by $t_{\min}$, the time where the experimental minimum creep rate appears. Although the initial creep rate is not accurately indicated by experiments, we can see that $\dot{\varepsilon}$ tends to decrease by a larger fraction when a lower stress or temperature is applied. As presented in Fig. 13a, such behavior is reproduced by the proposed model. Here the predicted strain curves (using the parameters listed in Table 1) are normalized by the strain rate at the first step of the simulations.

In the proposed model, the dynamic recovery process plays a key role in the evolution of dislocation population in the subgrain, which is responsible for capturing the tendency in experiments. Eq. 25 shows that the dynamic recovery parameter is a function of strain rate and the sensitivity is governed by n_0. According to Estrin [63], n_0 should be around 3-5 if climb is the dominant mechanism in dynamic recovery. For cross-slip controlled process, its value should be much higher (of order 20 as in Ref. [75]). In this work, $n_0 = 3.5$ is used in the simulations. Otherwise, the strain rate variance in the experimental data cannot be captured. In Fig. 13b, the simulation is carried out using $n_0 = 20$ and the parameter k_2 is set to 600 to fit the reference experimental results (700ºC and 150MPa). It shows that the predicted strain rate does not vary evidently under different loading conditions. This result implies dislocation

climb is the dominant mechanisms for dynamic recovery process in the conducted creep tests.

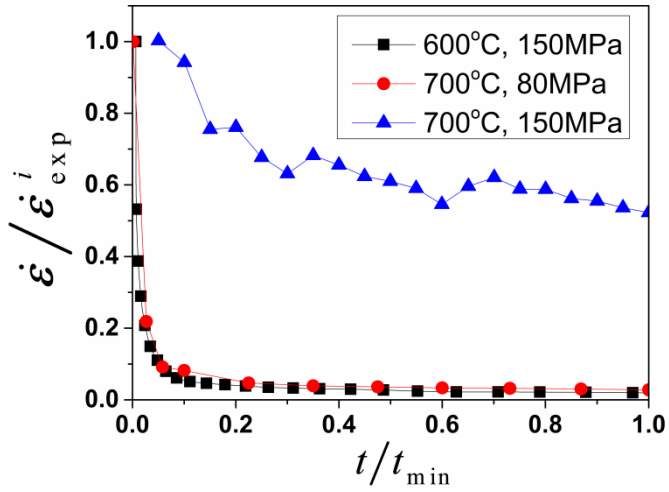

Fig. 12. Experimental creep rate evolution under different stresses and temperatures. Creep rate and time normalized by the initial creep rate and the time that the minimum creep rate presents respectively. Experimental data from Ref. [14].

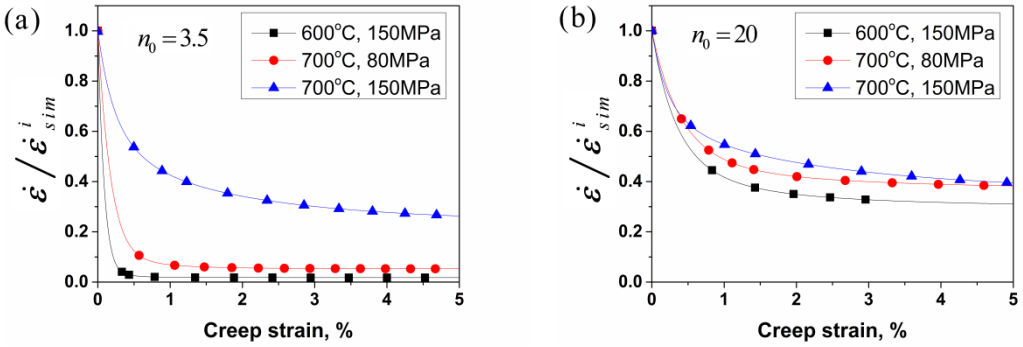

Fig. 13. Predicted creep rate evolution under different stresses and temperatures using $n_0 = 3.5$ (a) and $n_0 = 20$ (b). Creep rate normalized by the initial creep rate.

As mentioned in section 2.1, the growth of MX and $M_{23}C_6$ precipitates are neglected in this model, as well as the precipitations of Laves-phase and Z-phase. We believe this should not evidently affect the results in the present simulations. The experimental results in Basirat et al. [14] correspond to short term creep tests with a total creep time less than 200h. A rough estimate from the data in Ref. [7] indicates that the size of MX and $M_{23}C_6$ precipitates will grow less than 0.1% within this time range. Moreover, the study of Hayakawa et al. [4] shows that the dislocation mobility in modified 9Cr-1Mo steel is not significantly changed during creep tests up to around 7%

creep strain. This proves indirectly that the microstructure of this material is relatively stable for short-term tests.

4 Conclusions and perspectives

In this work, a crystallographic thermal creep model is proposed for Fe-Cr alloy. The thermal-activated glide and climb mechanisms are coupled in the formulation to determine the mean dislocation waiting time at different types of the obstacle (other dislocations and MX precipitates). This model, embedded in the VPSC framework, captures well the thermal creep behavior for modified 9Cr-1Mo steel under various stresses and temperatures. The relative contribution of thermally-activated glide and climb mechanisms is evaluated for different creep conditions. The results show that thermally-activated glide is strongly suppressed for creep at lower temperature, but makes a relatively higher contribution on the dislocation mobility in high-stress regime.

The dislocation density evolution law, considering multiple mechanisms in the annihilation process, is also essential to predict correctly the creep behavior for the initial and steady-state stages. The strain rate sensitive dynamic recovery is the dominant factor to capture the strain rate variance under various loading conditions.

In the next step, we will focus on exploring the potential of this model in connection with irradiation creep. This model describes the diffusion-controlled climb process through the gradient of vacancy concentration. In irradiation creep, the flux of defects reacting with the dislocation reaches the defect-dislocation reaction rate limit. There are several formulations available in the literature to express the climb velocity in this case, i.e. [22,76], which allow the extension of this model to predict the irradiation creep behavior for the cladding materials.

Appendix

Previous studies [18,44,50–52] show the climb velocity can be expressed as:

$$v_c^s = \frac{I_v^s \Omega}{b} \tag{A-1}$$

To calculate the vacancy current I_v^s, one needs to analyze the stress and vacancy concentration status around the climbing edge dislocation. A cylindrical control volume around the dislocation line with the radius r is defined. The zone with $r \le r_d$ is considered as the dislocation core region. Therefore the chemical force (Osmotic force) applied on the unit length of edge dislocation segment can be obtained as [44,77]:

$$f_{os}^s = -\frac{kTb}{\Omega} \ln\left(\frac{C_v^s(r_d)}{C_v^0}\right) \tag{A-2}$$

where $C^v(r_d)$ represents the vacancy concentration at $r = r_d$. C_v^0 is the equilibrium vacancy concentration at a given temperature.

Meanwhile, climb is also affected by the climb component of Peach-Koehler force. The full Peach-Koehler force is defined as $\boldsymbol{f} = \left(\boldsymbol{\sigma} \cdot \boldsymbol{b}^s\right) \times \boldsymbol{t}^s$ where $\boldsymbol{t}^s$ is the normalized tangent to the dislocation line [54,55]. The climb component of $\boldsymbol{f}$ for the edge dislocation can be expressed as [56–58]:

$$f_c^s = \boldsymbol{f}^s \cdot \boldsymbol{n}^s = \left[\left(\boldsymbol{\sigma} \cdot \boldsymbol{b}^s\right) \times \boldsymbol{t}^s\right] \cdot \boldsymbol{n}^s = -\left|\boldsymbol{b}^s\right| \boldsymbol{\sigma} : \left(\boldsymbol{b}^s \otimes \boldsymbol{b}^s\right) \tag{A-3}$$

When the dislocation is locally in equilibrium state, the total force $f^s = f_{os}^s + f_c^s$ should be equal to 0. Therefore we get from Eqs. A-2 and A-3:

$$C_v^s(\mathrm{r}_d) = C_{v,eq}^s = C_v^0 \exp\left(\frac{-f_c^s \Omega}{kTb}\right) \tag{A-4}$$

Notice that the vacancy concentration in the material matrix is assumed to be equal to the equilibrium concentration, $C_v(r \ge r_\infty) = C_v^\infty = C_v^0$, where r_∞ denotes the radius of the outer boundary for the control volume. Therefore a vacancy concentration gradient along the radius appears in the control volume which leads to a diffusive flow of vacancies. The dislocation needs to absorb or emit vacancies (climb) to retain the local equilibrium status.

At steady-state the divergence of vacancy diffusion flux J is null in the absence of defect creation. The associated Laplace equation in the cylindrical coordinate system is:

$$\nabla^2 C_v^s = \frac{1}{r}\frac{\partial}{\partial r} r \frac{\partial C_v^s}{\partial r} = 0 \tag{A-5}$$

with the inner and outer boundary conditions:

$$C_v^s(r{=}r_\infty) = C_v^\infty = C_v^0$$
$$C^v(r{=}r_d) = C_{v,eq}^s \tag{A-6}$$

By solving Eq. A-5, we obtain:

$$C_v^s(\mathrm{r}) = C_{v,eq}^s + (C_v^\infty - C_{v,eq}^s)\frac{\ln(\mathrm{r}/\,\mathrm{r}_\infty)}{\ln(\mathrm{r}_\infty/\,\mathrm{r}_d)} \tag{A-7}$$

Therefore, the net current absorbed or emitted by unit length of dislocation segment is given by:

$$I_v^s = 2\pi r \cdot J = 2\pi r \frac{D_v}{\Omega}\frac{\partial C_v^s(\mathrm{r})}{\partial r} = \frac{2\pi D_v\left[C_v^\infty - C_v^0 \exp\left(\frac{-f_c^s\Omega}{kTb}\right)\right]}{\Omega \ln(\mathrm{r}_\infty/\,\mathrm{r}_d)} \tag{A-8}$$

where D_v is the vacancy diffusivity. Then the climb velocity can be expressed as:

$$v_c^s = \frac{I_v^s\Omega}{b} = \frac{2\pi D_v\left[C_v^\infty - C_v^0 \exp\left(\frac{-f_c^s\Omega}{kTb}\right)\right]}{b\ln(\mathrm{r}_\infty/\,\mathrm{r}_d)} \tag{A-9}$$

References

[1] F. Abe, Precipitate design for creep strengthening of 9% Cr tempered martensitic steel for ultra- supercritical power plants Precipitate design for creep strengthening of 9% Cr tempered martensitic steel for ultra-supercritical power plants, Sci. Technol. Adv. Mater. 9 (2008) 13002–15.

[2] E. Cerri, E. Evangelista, S. Spigarelli, P. Bianchi, Evolution of microstructure in a modified 9Cr–1Mo steel during short term creep, Mater. Sci. Eng. A. 245 (1998) 285–292.

[3] H.K. Danielsen, Review of Z phase precipitation in 9–12 wt-%Cr steels, Mater. Sci. Technol. 0836 (2015) 1743284715Y.000.

[4] H. Hayakawa, S. Nakashima, J. Kusumoto, A. Kanaya, H. Nakashima, Creep deformation characterization of heat resistant steel by stress change test, Int. J. Press. Vessel. Pip. 86 (2009) 556–562.

[5] S. Yamasaki, Modelling Precipitation of Carbides in Martensitic Steels, 2009.

[6] K. Maruyama, K. Sawada, J. Koike, Strengthening mechanisms of creep resistant tempered martensitic steel, ISIJ Int. 41 (2001) 641–653.

[7] T. Nakajima, S. Spigarelli, E. Evangelista, T. Endo, Strain Enhanced Growth of

Precipitates during Creep of T91, Mater. Trans. 44 (2003) 1802–1808.

[8] J. Hald, Microstructure and long-term creep properties of 9-12% Cr steels, Int. J. Press. Vessel. Pip. 85 (2008) 30–37.

[9] Y. Yamamoto, B.A. Pint, K.A. Terrani, K.G. Field, Y. Yang, L.L. Snead, Development and property evaluation of nuclear grade wrought FeCrAl fuel cladding for light water reactors, J. Nucl. Mater. 467 (2015) 703–716.

[10] K.G. Field, M.N. Gussev, Y. Yamamoto, L.L. Snead, Deformation behavior of laser welds in high temperature oxidation resistant Fe-Cr-Al alloys for fuel cladding applications, J. Nucl. Mater. 454 (2014) 352–358.

[11] K.G. Field, X. Hu, K.C. Littrell, Y. Yamamoto, L.L. Snead, Radiation tolerance of neutron-irradiated model Fe-Cr-Al alloys, J. Nucl. Mater. 465 (2015) 746–755.

[12] T. Shrestha, M. Basirat, I. Charit, G.P. Potirniche, K.K. Rink, Creep rupture behavior of Grade 91 steel, Mater. Sci. Eng. A. 565 (2013) 382–391.

[13] T. Shrestha, M. Basirat, I. Charit, G.P. Potirniche, K.K. Rink, U. Sahaym, Creep deformation mechanisms in modified 9Cr-1Mo steel, J. Nucl. Mater. 423 (2012) 110–119.

[14] M. Basirat, T. Shrestha, G.P. Potirniche, I. Charit, K. Rink, A study of the creep behavior of modified 9Cr-1Mo steel using continuum-damage modeling, Int. J. Plast. 37 (2012) 95–107.

[15] M. Tamura, H. Sakasegawa, A. Kohyama, H. Esaka, K. Shinozuka, Effect of MX type particles on creep strength of ferritic steel, J. Nucl. Mater. 321 (2003) 288–293.

[16] M. Taneike, F. Abe, K. Sawada, Creep-strengthening of steel at high temperatures using nano-sized carbonitride dispersions., Nature. 424 (2003) 294–296.

[17] S. Spigarelli, E. Cerri, P. Bianchi, E. Evangelista, Materials Science and Technology Interpretation of creep behaviour of a 9Cr–Mo–Nb–V–N (T91) steel using threshold stress concept Interpretation of creep behaviour of a 9Cr–Mo–Nb–V–N (T91) steel using threshold stress concept, (2016).

[18] G.S. Was, Fundamentals of radiation materials science: metals and alloys, Springer Science & Business Media, 2007.

[19] E. Arzt, J. Rosler, The kinetics of dislocation climb over hard particles-II. Effects of an attractive particle-dislocation interaction, Acta Metall. 36 (1988) 1053–1060.

[20] E. Arzt, D.S. Wilkinson, Threshold stresses for dislocation climb over hard particles: The effect of an attractive interaction, Acta Metall. 34 (1986) 1893–1898.

[21] J. Roesler, E. Arzt, The kinetics of dislocation climb over hard particles - i. Climb without attractive particle-dislocation interaction, Acta Metall. 36 (1988) 1043–1051.

[22] A. Patra, D.L. McDowell, Crystal plasticity-based constitutive modelling of irradiated bcc structures, Philos. Mag. 92 (2012) 861–887.

[23] Y. Qin, G. Götz, W. Blum, Subgrain structure during annealing and creep of the cast martensitic Cr-steel G-X12CrMoWVNbN 10-1-1, Mater. Sci. Eng. A. 341 (2003) 211–215.

[24] E. Nes, Modelling of work hardening and stress saturation in FCC metals, Prog. Mater. Sci. 41 (1997) 129–193.

[25] Y. Estrin, H. Mecking, A unified phenomenological description of work hardening and creep based on one-parameter models, Acta Metall. 32 (1984) 57–70.

[26] B. Reichert, Y. Estrin, H. Schuster, Implementation of Precipitation and Ripening of Second-Phase Particles in the Constitutive Modelling of Creep, Scr. Mater. 38 (1998) 1463–1468.

[27] G. Gottstein, A.S. Argon, Dislocation theory of steady state deformation and its approach in creep and dynamic tests, Acta Metall. 35 (1987) 1261–1271.

[28] F. Roters, D. Raabe, G. Gottstein, Work hardening in heterogeneous alloys—a microstructural approach based on three internal state variables, Acta Mater. 48 (2000) 4181–4189.

[29] Y. Xiang, D.J. Srolovitz, Dislocation climb effects on particle bypass mechanisms, Philos. Mag. 86 (2006) 3937–3957.

[30] R. Oruganti, A new approach to dislocation creep, Acta Mater. 60 (2012) 1695–1702.

[31] R.A. Lebensohn, C.N. Tomé, A self-consistent anisotropic approach for the simulation of plastic deformation and texture development of polycrystals: Application to zirconium alloys, Acta Metall. Mater. 41 (1993) 2611–2624.

[32] R.A. Lebensohn, C.N. Tomé, P.P. CastaÑeda, Self-consistent modelling of the mechanical behaviour of viscoplastic polycrystals incorporating intragranular field fluctuations, Philos. Mag. 87 (2007) 4287–4322.

[33] B. Fournier, M. Sauzay, A. Pineau, Micromechanical model of the high temperature cyclic behavior of 9-12%Cr martensitic steels, Int. J. Plast. 27 (2011) 1803–1816.

[34] H. Wang, B. Clausen, L. Capolungo, I.J. Beyerlein, J. Wang, C.N. Tomé, Stress and strain relaxation in magnesium AZ31 rolled plate: In-situ neutron measurement and elastic viscoplastic polycrystal modeling, Int. J. Plast. 79 (2016) 275–292.

[35] H. Wang, L. Capolungo, B. Clausen, C.N. Tomé, A crystal plasticity model based on transition state theory, Int. J. Plast. (2016).

[36] J.T. Lloyd, J.D. Clayton, R.A. Austin, D.L. McDowell, Plane wave simulation of elastic-viscoplastic single crystals, J. Mech. Phys. Solids. 69 (2014) 14–32.

[37] R.J. Clifton, Analysis of elastic-visco-plastic waves of finite uniaxial strain, (1971).

[38] R.A. Austin, D.L. McDowell, A dislocation-based constitutive model for viscoplastic deformation of fcc metals at very high strain rates, Int. J. Plast. 27 (2011) 1–24.

[39] N. Bertin, C.N. Tomé, I.J. Beyerlein, M.R. Barnett, L. Capolungo, On the strength of dislocation interactions and their effect on latent hardening in pure Magnesium, Int. J. Plast. 62 (2014) 72–92.

[40] C. Sobie, N. Bertin, L. Capolungo, Analysis of Obstacle Hardening Models Using Dislocation Dynamics: Application to Irradiation-Induced Defects, Metall. Mater. Trans. A Phys. Metall. Mater. Sci. 46 (2015) 3761–3772.

[41] G.E. Lucas, The evolution of mechanical property change in irradiated austenitic stainless steels, J. Nucl. Mater. 206 (1993) 287–305.

[42] C. Deo, C. Tomé, R. Lebensohn, S. Maloy, Modeling and simulation of irradiation hardening in structural ferritic steels for advanced nuclear reactors, J. Nucl. Mater. 377 (2008) 136–140.

[43] J. Friedel, Electron Microscopy Strength Crystals, in: Wiley, New York, 1963: p. 605.

[44] J.P. Hirth, J. Lothe, Theory of Dislocations (2nd ed.), J. Appl. Mech. 50 (1983) 476.

[45] V. Gaffard, Experimental study and modelling of high temperature creep flow and damage behaviour of 9Cr1Mo-NbV steel weldments, 2004.

[46] U.F. Kocks, A.S. Argon, M.F. Ashby, Thermodynamics and Kinetics of Slip, Prog. Mater. Sci. 19 (1975) 171–229.

[47] U. Lagerpusch, V. Mohles, D. Baither, B. Anczykowski, E. Nembach, Double strengthening of copper by dissolved gold-atoms and by incoherent SiO2-particles: How do the two strengthening contributions superimpose?, Acta Mater. 48 (2000) 3647–3656.

[48] Y. Dong, T. Nogaret, W.A. Curtin, Scaling of dislocation strengthening by multiple obstacle types, Metall. Mater. Trans. A Phys. Metall. Mater. Sci. 41 (2010) 1954–1960.

[49] A. V. Granato, K. Lücke, J. Schlipf, L.J. Teutonico, Entropy Factors for Thermally Activated Unpinning of Dislocations, J. Appl. Phys. 35 (1964) 2732.

[50] M.G.D. Geers, M. Cottura, B. Appolaire, E.P. Busso, S. Forest, A. Villani, Coupled glide-climb diffusion-enhanced crystal plasticity, J. Mech. Phys. Solids. 70 (2014) 136–153.

[51] B. Bakó, E. Clouet, L.M. Dupuy, M. Blétry, Dislocation dynamics simulations with climb: kinetics of dislocation loop coarsening controlled by bulk diffusion, Philos. Mag. 91 (2011) 3173–3191.

[52] Y. Gu, Y. Xiang, S.S. Quek, D.J. Srolovitz, Three-dimensional formulation of dislocation climb, J. Mech. Phys. Solids. 83 (2014) 319–337.

[53] D. Mordehai, E. Clouet, M. Fivel, M. Verdier, Introducing dislocation climb by bulk diffusion in discrete dislocation dynamics, Philos. Mag. 88 (2008) 899–925.

[54] J. Weertman, The Peach–Koehler equation for the force on a dislocation modified for hydrostatic pressure, Philos. Mag. 11 (1965) 1217–1223.

[55] J. Weertman, J.R. Weertman, Elementary Dislocation Theory, Oxford University Press, Oxford, 1992.

[56] R. a. Lebensohn, C.S. Hartley, C.N. Tomé, O. Castelnau, Modeling the mechanical response of polycrystals deforming by climb and glide, Philos. Mag. 90 (2010) 567–583.

[57] R.A. Lebensohn, R.A. Holt, A. Caro, A. Alankar, C.N. Tomé, Improved constitutive description of single crystal viscoplastic deformation by dislocation climb, Comptes Rendus - Mec. 340 (2012) 289–295.

[58] C.S. Hartley, A method for linking thermally activated dislocation mechanisms of yielding with continuum plasticity theory, Philos. Mag. 83 (2003) 3783–3808.

[59] J. Chang, W. Cai, V. V Bulatov, S. Yip, Dislocation Motion in BCC Metals by Molecular Dynamics, Mater. Sci. Eng. A. 309-310 (2001) 160–163.

[60] W. Wen, M. Borodachenkova, C.N. Tomé, G. Vincze, E.F. Rauch, F. Barlat, J.J. Grácio, Mechanical behavior of low carbon steel subjected to strain path changes: Experiments and modeling, Acta Mater. 111 (2016) 305–314.

[61] W. Wen, M. Borodachenkova, C.N. Tomé, G. Vincze, E.F. Rauch, F. Barlat, J.J. Grácio, Mechanical behavior of Mg subjected to strain path changes: Experiments and modeling, Int. J. Plast. 73 (2015) 171–183.

[62] K. Kitayama, C.N. Tomé, E.F. Rauch, J.J. Gracio, F. Barlat, A crystallographic dislocation model for describing hardening of polycrystals during strain path changes. Application to low carbon steels, Int. J. Plast. 46 (2013) 54–69.

[63] Y. Estrin, Dislocation theory based constitutive modelling: foundations and applications, J. Mater. Process. Technol. 80-81 (1998) 33–39.

[64] U.F. Kocks, H. Mecking, Physics and phenomenology of strain hardening: The FCC case, Prog. Mater. Sci. 48 (2003) 171–273.

[65] H. Mecking, U.F. Kocks, Kinetics of flow and strain-hardening, Acta Metall. 29 (1981) 1865–1875.

[66] I.J. Beyerlein, C.N. Tome, A dislocation-based constitutive law for pure Zr including temperature effects, Int. J. Plast. 24 (2008) 867–895.

[67] U.F. Kocks, A statistical theory of flow stress and work-hardening, Philos. Mag. 13 (1966) 541–566.

[68] H. Wang, B. Raeisinia, P.D. Wu, S.R. Agnew, C.N. Tomé, Evaluation of self-consistent polycrystal plasticity models for magnesium alloy AZ31B sheet, Int. J. Solids Struct. 47 (2010) 2905–2917.

[69] S. Queyreau, G. Monnet, B. Devincre, Slip systems interactions in α-iron determined by dislocation dynamics simulations, Int. J. Plast. 25 (2009) 361–377.

[70] C.G. Panait, A. Zielińska-Lipiec, T. Koziel, A. Czyrska-Filemonowicz, A.-F. Gourgues-Lorenzon, W. Bendick, Evolution of dislocation density, size of subgrains and MX-type precipitates in a P91 steel during creep and during thermal ageing at 600°C for more than 100,000h, Mater. Sci. Eng. A. 527 (2010) 4062–4069.

[71] S. Hollner, B. Fournier, J. Le Pendu, T. Cozzika, I. Tournié, J.C. Brachet, A. Pineau, High-temperature mechanical properties improvement on modified 9Cr-1Mo martensitic steel through thermomechanical treatments, J. Nucl. Mater. 405 (2010) 101–108.

[72] M.I. Mendelev, Y. Mishin, Molecular dynamics study of self-diffusion in bcc Fe, Phys. Rev. B - Condens. Matter Mater. Phys. 80 (2009) 1–9.

[73] V. Gaffard, A.F. Gourgues-Lorenzon, J. Besson, High temperature creep flow and damage properties of 9Cr1MoNbV steels: Base metal and weldment, Nucl. Eng. Des. 235 (2005) 2547–2562.

[74] G. Monnet, Multiscale modeling of precipitation hardening: Application to the Fe–Cr alloys, Acta Mater. 95 (2015) 302–311.

[75] J. Li, A.K. Soh, Modeling of the plastic deformation of nanostructured materials with grain size gradient, Int. J. Plast. 39 (2012) 88–102.

[76] V.I. Dubinko, New mechanism of irradiation creep based on the radiation-induced vacancy emission from dislocations, Radiat. Eff. Defects Solids. 160 (2005) 85–97.

[77] H. Wiedersich, K. Herschbach, The concept of “chemical stress” caused by arbitrary vacancy and interstitial supersaturations, Scr. Metall. 6 (1972) 453–457.